Binding Kinetics and Lateral Mobility of HSV-1 on End-Grafted Sulfated Glycosaminoglycans

Citation for the original published paper (version of record):
Peerboom, N., Block, S., Altgärde, N. et al (2017). Binding Kinetics and Lateral Mobility of HSV-1 on End-Grafted Sulfated Glycosaminoglycans. Biophysical Journal, 113(6): 1223-1234.
http://dx.doi.org/10.1016/j.bpj.2017.06.028

Biophysical Journal
Article

Biophysical Society

Binding Kinetics and Lateral Mobility of HSV-1 on End-Grafted Sulfated Glycosaminoglycans

Nadia Peerboom,[1] Stephan Block,[1,2] Noomi Altgärde,[1] Olov Wahlsten,[1] Stephanie Möller,[3] Matthias Schnabelrauch,[3] Edward Trybala,[4] Tomas Bergström,[4] and Marta Bally[1,*]
[1]Department of Physics, Chalmers University of Technology, Göteborg, Sweden; [2]Department of Chemistry and Biochemistry, Freie Universität Berlin, Berlin, Germany; [3]Department of Biomaterials, INNOVENT e.V., Jena, Germany; and [4]Department of Infectious Diseases, Institute of Biomedicine, University of Gothenburg, Göteborg, Sweden

ABSTRACT Many viruses, including herpes simplex (HSV), are recruited to their host cells via interaction between their envelope glycoproteins and cell-surface glycosaminoglycans (GAGs). This initial attachment is of a multivalent nature, i.e., it requires the establishment of multiple bonds between amino acids of viral glycoproteins and sulfated saccharides on the GAG chain. To gain understanding of how this binding process is modulated, we performed binding kinetics and mobility studies using end-grafted GAG chains that mimic the end attachment of these chains to proteoglycans. Total internal reflection fluorescence microscopy was used to probe binding and release, as well as the diffusion of single HSV-1 particles. To verify the hypothesis that the degree of sulfation, but also the arrangement of sulfate groups along the GAG chain, plays a key role in HSV binding, we tested two native GAGs (chondroitin sulfate and heparan sulfate) and compared our results to chemically sulfated hyaluronan. HSV-1 recognized all sulfated GAGs, but not the nonsulfated hyaluronan, indicating that binding is specific to the presence of sulfate groups. Furthermore we observed that a notable fraction of GAG-bound virions exhibit lateral mobility, although the multivalent binding to the immobilized GAG brushes ensures firm virus attachment to the interface. Diffusion was faster on the two native GAGs, one of which, chondroitin sulfate, was also characterized by the highest association rate per GAG chain. This highlights the complexity of multivalent virus-GAG interactions and suggests that the spatial arrangement of sulfates along native GAG chains may play a role in modulating the characteristics of the HSV-GAG interaction. Altogether, these results, obtained with a minimal and well-controlled model of the cell membrane, provide, to our knowledge, new insights into the dynamics of the HSV-GAG interaction.

INTRODUCTION

The recruitment of viral pathogens to susceptible host cells is often mediated by the carbohydrates exposed on the cell membrane (1). Many viruses, including the human immunodeficiency virus (2), the Ebola virus (3), the human papillomavirus (4), and the Zika virus (5), take advantage of sulfated glycosaminoglycans (GAGs) attached to cell-associated proteoglycans to initiate cell infection. This is also the case for herpes simplex virus type 1 (HSV-1), a ubiquitous human pathogen, causing mucocutaneous lesions on lips and mouth (6) but also, in rare cases, severe encephalitis (7). Initial attachment of HSV-1 is mediated by the envelope glycoprotein gC binding to heparan sulfate (HS) (8) and chondroitin sulfate (CS) (9,10), two sulfated GAGs found on the cell surface and in the extracellular matrix. Furthermore, glycoprotein gB has been shown to take over the role of attachment protein in gC-deficient virions (11). The GAG-binding site of gC-1 (gC of HSV-1) has been identified as a cluster of positive and hydrophobic residues situated close to the N-terminal protein region (10,12,13). On the GAG side, the interaction is often believed to be of a rather nonspecific nature, as it involves multiple electrostatic interactions mediated in the first place by negatively charged sulfate groups. However, many GAG-binding proteins show remarkable specificity by targeting either unique modifications or domain structures within the GAG chains (14). Indeed, for gC binding to HS, preferential binding to specific carbohydrate sequences has been reported, indicating that HSV-HS interactions can exhibit some degree of specificity (15,16).

Virus-GAG interactions are characterized by an immense complexity. They involve the simultaneous establishment of a multitude of relatively weak (17) protein-carbohydrate interactions, which need to act in concert and with high spatiotemporal organization to mediate the processes leading to virus uptake or egress. These multivalent interactions allow

Submitted January 18, 2017, and accepted for publication June 14, 2017.
*Correspondence: bally@chalmers.se
Editor: Kalina Hristova.
http://dx.doi.org/10.1016/j.bpj.2017.06.028

for a tight control of the nature of the interaction, including modulation of affinity and specificity or of the diffusive properties of the virus on the surface (18,19). For example, the initial attachment of a virus to the cell surface is often of weak nature, followed by the establishment of multiple interactions between several viral attachment proteins and cellular receptor molecules, which ensure stable adhesion (18). The complexity of GAG-mediated interactions, in particular those involving the sulfated species HS and CS, also stems from the heterogeneous nature of the carbohydrate chains, which are sulfated in complex and dynamic enzymatic pathways. This results in a highly heterogeneous distribution, not only of carbohydrate chains with different physicochemical properties on the cell surface (20), but also of the sulfate groups along individual GAG chains. In particular for HS, sulfation occurs in patterns with unsulfated domains and highly sulfated domains alternating along the GAG chains (21,22). Such distinct sulfation patterns have been found to be specific for certain tissues, development stages, and disease conditions (23,24). Moreover, this domain structure has been speculated to play an important role in increasing the specificity of GAG-protein interactions (25,26). Finally, it has also been shown to influence virus binding, since specific structural features on the HS chain have been shown to interact with HSV-1, for example (15).

For many GAG-binding viruses, including HSV-1, the process of initial attachment to the cell surface is far from being fully understood. Although the main actors in this process (viral glycoproteins and cell-surface GAGs) have been identified, very little is known about the dynamics of the virus-GAG interaction. It is, for example, unclear which mechanisms viruses employ to travel through the extracellular matrix and along the cell surface before firmly attaching to it and proceeding with cell entry. Identifying characteristic behaviors and thereby gaining further knowledge about the processes modulating the interaction between virus and cell surface is, however, a key step toward the development of new anti-viral therapies and vaccines.

One of the major challenges in identifying dynamic processes relevant to virus attachment and entry is the large heterogeneity of virus samples, which consist of individual virions of distinct physicochemical properties. Accordingly, important behavioral differences might only be represented by small subpopulations of the studied sample and only a small fraction of a given virus population successfully replicates inside the host organism. This calls for the use of techniques able to resolve binding properties on a single-particle level. This is not possible with classical ensemble averaging techniques, justifying the recent trend toward the use of single-particle-based techniques in virus research (27–29).

The aim of this study was to investigate the influence of the physicochemical properties of sulfated GAGs on mobility and binding kinetics of single HSV-1 virions. To this end, we used a model of the cell surface based on GAG chains end-grafted to a sensor surface. Our model mimics the attachment of GAG chains to the proteoglycan core proteins, and has the advantage of allowing controlled alterations in surface properties. Although surface plasmon resonance (SPR) served to monitor and characterize the surface functionalization, we opted for a single-particle approach to resolve binding and diffusion characteristics of single HSV-1 virions. Binding to the functionalized surfaces was recorded using total internal reflection fluorescence (TIRF) microscopy. From the recorded movies, we extracted information on HSV mobility using single-particle tracking (SPT), and on binding kinetics using equilibrium fluctuation analysis (30,31).

MATERIALS AND METHODS

Materials

All materials were purchased from commercial sources, unless stated otherwise. We obtained 1-palmitoyl-2-oleoyl-*sn*-glycero-3-phosphocholine (POPC) and 1,2-dioleoyl-*sn*-glycero-3-phosphoethanolamine-N-(cap biotinyl) (sodium salt) (DOPE-biotin) from Avanti Polar Lipids (Alabaster, AL). Poly-L-lysine-grafted-polyethylene glycol (PLL-g-PEG and PLL-g-PEG-biotin) was purchased from SuSoS AG (Dübendorf, Switzerland). Phosphate-buffered saline (PBS, tablets), streptavidin (SA), and PKH26 red fluorescent cell linker kit (containing PKH26 dye and diluent C) were purchased from Sigma-Aldrich (Munich, Germany). SA, Alexa Fluor 488 conjugate was obtained from Thermo Fisher Scientific (Stockholm, Sweden) and illustra MicroSpin S-200 HR columns from GE Healthcare (Danderyd, Sweden). PBS was filtered with Whatman (Maidstone, United Kingdom) filters (0.2 μm) before use (GE Healthcare, Little Chalfont, United Kingdom). In addition, for the SPR experiments, PBS was degassed using an Elmasonic (Singen, Germany) S40H sonicator. Water was deionized and filtered using a Milli-Q system (Millipore, Molsheim, France).

GAG derivatives

A summary of the end-biotinylated GAGs used in this study together with their characteristics is given in Table 1. The GAGs were obtained from commercial sources (HA was from Aqua Biochem, Dessau, Germany; CS was from Kraeber, Ellerbek, Germany; and HS was from Celsus Laboratories, Cincinnati, OH). Low-molecular-weight hyaluronan (HA) was prepared as described in (32) and served as starting material for synthetically sulfated hyaluronan (sHA) (33). CS was a mixture of 70% chondroitin-4-sulfate and 30% chondroitin-6-sulfate. HS was derived from porcine intestinal mucosa and conjugated with biotin at their reducing end via oxime ligation (34). HA, sHA, and CS were derivatized at their

TABLE 1 Glycosaminoglycan Derivatives Used in This Study

Name	Abbreviation	Molecular Mass (kDa)	n[a]	$DS_{Sulfate}$[b]
Hyaluronan	HA	23	57	0
Sulfated hyaluronan	sHA	30	42	3.1
Chondroitin sulfate	CS	20	41	0.9
Heparan sulfate	HS	12	22	1.4

[a]Average number of disaccharide units per GAG chain, estimated from the average molecular weight.
[b]Average number of sulfate groups per disaccharide unit obtained by elemental analysis (33,74).

reducing end via biotin-LC-hydrazide coupling (35). The GAG chains were between ~20 and ~60 nm long.

Lipid vesicle preparation

POPC and DOPE-biotin lipids were dissolved and stored in chloroform. A total mass of 2 mg was mixed as a ratio of 1 wt % DOPE-biotin in POPC and dried at the bottom of a round glass flask under gentle N_2 flow. The flask was kept under vacuum for >1 h to remove residual chloroform. Lipids were then hydrated in 1 mL filtered PBS and vortexed until no traces of lipids remained visible on the glass (~1 min). The 2 mg/mL lipid solution was extruded 11 times through a 30 nm polycarbonate membrane (Whatman) using a mini extruder (Avanti Polar Lipids).

Virus purification and fluorescent labeling

The virus strain HSV-1 KOS (VR-1493; ATCC, Manassas, VA) (36) was purified from infectious culture media of GMK AH1 cells through a three-step discontinuous sucrose gradient, as described in (37). The purified solution was stored as aliquots of 25 μL at −80°C until use. The amount of infectious particles, in terms of plaque forming units (PFUs), was determined with a viral plaque titration assay (37), yielding 6×10^9 PFU/mL. Viral DNA from HSV-1 was extracted and quantified through real-time quantitative PCR, as further described in (38). The obtained DNA count value was 8.1×10^{10} mL^{-1}. A size distribution of the virus suspension was obtained with nanoparticle tracking analysis (NTA) (Fig. S1), showing a main peak with a mean diameter of 225 nm, in agreement with values reported in the literature (39).

The virus suspension was fluorescently labeled using PKH26 red fluorescent cell linker dye and diluent C, a diluting agent provided in the labeling kit. Then, 3 μL of dye (0.5 mM in ethanol) were mixed with 25 μL of virus solution using 500 μL of diluent C diluting agent. Dye and virus were incubated for 10 min on ice and protected from light. The mixture was then centrifuged for 1 min at 2000 × *g* through illustra MicroSpin columns to remove excess dye. The obtained solution was diluted 10 times in PBS before injection.

MP-SPR

An SPR Navi 220A (Bionavis, Tampere, Finland) was used to perform SPR measurements. SiO_2-coated chips (SPR102-SIO2, Bionavis) were stored overnight in sodium dodecyl sulfate (SDS; Sigma-Aldrich) and rinsed with Milli-Q water. The chips were then cleaned for 15 min with ultraviolet-ozone. Measurements were performed at 22°C using two wavelengths (670 and 785 nm). The running buffer was PBS.

SLBs were formed on the cleaned SiO_2 chips by running a 0.1 mg/mL POPC + 1 wt % DOPE-biotin solution through the flow cells. SA was then bound to the biotin groups incorporated in the bilayer (25 μg/mL solution). Biotinylated HA and sHA were immobilized on the SLB + SA layer (0.1 mg/mL solution). Biotinylated CS and HS were injected at concentrations of 0.5 and 0.1 mg/mL, respectively. All solutions were prepared in PBS.

Surface coverages presented in Table 2 were estimated using Eq. 1 under the thin film approximation (40,41):

$$\Delta\Gamma = \frac{\delta}{S\,(\mathrm{d}n/\mathrm{d}C)}\Delta\mathrm{deg}, \quad (1)$$

where δ is the decay length of the intensity of the evanescent field, S is the sensitivity of the instrument expressed in degrees per refractive index unit, and $(\mathrm{d}n/\mathrm{d}C)$ is the refractive index increment per biomolecule concentration in solution. The thin film approximation describes the case where the adsorbed film thickness is much smaller than the decay length, δ, and can therefore readily be applied to calculate the adsorbed mass of the lipid bilayer and the SA layer. For the calculations of the surface coverage of the GAG layer, this approximation can lead to an error of up to 30% in the case of a fully stretched out GAG molecule of 60 nm in length. However, since the GAG-film thickness is likely to be significantly smaller than the extended length of a GAG molecule, we expect the predicted error to be much smaller. We used Eq. 1 with a decay length of 109 at 670 nm (42), and the sensitivity at 670 nm has been measured to be 109.68 deg/dn using a reference sample. Average values of $\mathrm{d}n/\mathrm{d}C$ were obtained from the literature: lipids were 0.18 mL/g (43), SA was 0.18 mL/g (44), HA was 0.16 mL/g (45), CS and sHA were 0.147 mL/g (44,46,47), and HS was 0.132 mL/g (48–50). All results were averaged over $n \geq 3$ observations, and all error intervals indicate standard deviations.

TIRF microscopy

Microscope cover glasses (24 × 40 mm^2; Fisherbrand, Fisher Scientific, Waltham, MA) were boiled for >1 h in a 10% 7× detergent/Milli-Q solution (MP Biomedicals, Santa Ana, CA) and stored in Milli-Q water until use. The glasses were rinsed with Milli-Q water and dried under N_2 flow right before use. Microwells were formed by attaching a thin rectangular piece of polydimethylsiloxane (PDMS), made from a mixture of 10:1 Sylgard 184 and curing agent (Dow Corning, Midland, MI), onto the glass. The PDMS piece contained nine holes of ~18 μL volume each, and was stored between regular office tape to avoid contamination, and to possibly enhance its adhesion to glass.

SLBs were formed on the cleaned cover glasses by adding 10 μL of 0.5 mg/mL POPC + 1 wt% DOPE-biotin vesicles to the microwells. After 20–30 min of incubation, 5 μL were removed from the wells and the remaining solution was rinsed 10 times with 15–20 μL of PBS. 5 μL of 0.5 mg/mL SA were added to ~5 μL of remaining solution and incubated for 20 min. The same rinsing process was repeated and 5 μL of biotinylated GAGs (HA, sHA: 0.2 mg/mL; CS: 1 mg/mL; HS: 0.1 mg/mL) were added to ~5 μL of PBS followed by another rinsing step performed as described above. 10 μL of the labeled virus suspension were finally added to the well containing 5 μL of PBS and incubated for ~60 min before the start of the

TABLE 2 SPR Response, Estimated Optical Mass, Surface Coverage, Average Spacing, and Density of Sulfate Groups for the Different GAG Immobilization Steps

	SPR Response (670 nm) (°)	Optical Mass (ng/cm^2)	Surface Coverage[a] (10^{11}/cm^2)	Average Spacing[b] (nm)	Density of Sulfate Groups (10^{12}/cm^2)
Bilayer (step i)[c]	0.755 ± 0.017	417.0 ± 9.4	/	/	/
SA (step ii)[c]	0.247 ± 0.007	136.4 ± 4.1	13.7 ± 0.4	8.6 ± 0.1	/
HA (step iii)[c]	0.072 ± 0.012	44.6 ± 7.6	11.7 ± 2.0	9.4 ± 0.8	/
sHA (step iii)[c]	0.029 ± 0.002	19.8 ± 1.3	4.0 ± 0.3	15.9 ± 0.5	51.7 ± 3.3
CS (step iii)[c]	0.012 ± 0.004	7.9 ± 2.6	2.4 ± 0.8	21.3 ± 3.6	8.8 ± 2.9
HS (step iii)[c]	0.049 ± 0.002	37.3 ± 1.4	18.7 ± 0.7	7.3 ± 0.1	57.6 ± 2.2

[a]Assuming that the average molecular mass of surface-bound GAGs is the same as in solution.
[b]Calculated as root mean-square (RMS) spacing.
[c]See Fig. 1 for a definition of the GAG immobilization steps.

measurements. All solutions were prepared in PBS. For the control experiment using 5% biotin, we used vesicles of POPC + 5 wt% DOPE-biotin instead of the vesicles stated above. For the PLL-g-PEG system, we added 10 μL of 0.1 mg/mL PLL-g-PEG + 20 vol% PLL-g-PEG/PEG-biotin) instead of the vesicles to the microwells. All following steps of the surface functionalization were kept identical.

A Nikon Eclipse Ti-E inverted microscope (Nikon Corporation, Minato, Japan) was used together with a 60× oil immersion objective (NA = 1.49) to record time-lapse movies (1.5 s time interval/750 frames) for both equilibrium fluctuation analysis and SPT studies. The microscope was equipped with an Andor DU879E-CSBV camera (Andor Technology, Belfast, UK), an X-Cite 120 light source (Lumen Dynamics Group, Mississauga, Canada), and a TRITC filter cube (Nikon).

SPT

All SPT data analysis was done using homemade scripts written in MATLAB (The MathWorks, Natick, MA). Tracking was implemented using local nearest-neighbor linking (51), while the dependence between mean-square displacement (MSD) and lag time (Δt) was calculated for each observed track using the internal averaging procedure (52). Since the obtained MSD-Δt curves of single virus particles did not always increase linearly with Δt (as expected for normal diffusion) but showed indications of anomalous diffusion in a notable fraction of observed trajectories, all MSD-Δt curves were fitted using both a model for normal diffusion,

$$\mathrm{MSD}(\Delta t) = 4D\Delta t + \sigma_0, \quad (2)$$

and a model for confined diffusion (53,54),

$$\mathrm{MSD}(\Delta t) = \frac{L_C^2}{3}\left(1 - \exp\left[-\frac{12D_C\Delta t}{L_C^2}\right]\right) + \sigma_0, \quad (3)$$

with D and D_C denoting the extracted diffusion coefficients for normal or anomalous diffusion, respectively, L_C the length scale of confinement (in the case of anomalous diffusion; see Fig. S2 for L_C distributions), and σ_0 the vertical offset of the MSD curve from zero (caused by the error done in localizing the virus position in the TIRF movies due to localization noise). Note that we refer here to anomalous diffusion in its most generic definition, i.e., diffusion leading to MSD curves showing a nonlinear dependence of Δt.

Tracked virus particles were assigned to anomalous diffusion if their corresponding MSD-Δt curves were better described by Eq. 3 than Eq. 2 (indicated by a smaller root mean-square error caused by the fit); elsewise, they were assigned to normal diffusion. As Eq. 2 can be obtained from Eq. 3 by Taylor expansion in the limit of large L_C values, fitting Eqs. 2 and 3 to a linear MSD curve (normal diffusion) will give almost identical fitting errors. As a consequence, to be assigned to anomalous diffusion behavior, an MSD curve needs to be sufficiently nonlinear to yield a lower fitting error of Eq. 3 with respect to Eq. 2. Although Eq. 3 described the MSD curves of corralled diffusion of particles (confined in an area with length scale L_C), Eq. 3 is used here without loss of generality, as only the extracted D_C values will be employed for further analysis in this work. These values correspond to the slope of the corresponding MSD curves in the limit of infinitesimal Δt values and could also be derived, without any assumption on the underlying diffusion process, by fitting a linear relationship (such as Eq. 2) to the MSD curves for small Δt. Nevertheless, the latter approach requires that we define a suitable upper limit for Δt, whereas Eq. 3 can be applied to the entire MSD curve, thereby avoiding introduction of additional thresholds and also increasing the fitting accuracy (as the fit is based on more data points). Hence, fitting the MSD curves using Eqs. 2 and 3 allows the complex diffusion behavior of HSV-1 to be quantified (by D and D_C values, respectively) within a single framework, without loss of generality or introduction of thresholds that are usually employed to distinguish normal from anomalous diffusion.

Finally, the ratio of particles exhibiting anomalous diffusion was calculated as the number of tracks assigned to anomalous diffusion divided by the total number of tracks. Peak values of the distribution of diffusion coefficients were determined for the immobile and mobile peaks of both anomalous and normal diffusion. Mobile fractions were calculated as the number of tracks in the mobile peak divided by the total number of tracks. All values were averaged over $n \geq 3$ observations (see Table S1 for complete statistical information) and reported as the mean ± SE.

Equilibrium fluctuation analysis

To quantify binding and release kinetics of individual virus particles, the recorded time-lapse movies were analyzed with a method called equilibrium fluctuation analysis (30). MATLAB scripts were written in house. With this method, only particles with an intensity higher than a set threshold (th_high) and a pixel size (rem_size) >3 were detected. Particles were considered as firmly bound if present for at least $t_{min} = 10$ frames and considered as dissociated if the pixel intensity at the centroid position dropped below a low threshold (th_low). Threshold values were set manually after visual inspection of the movies; the values were the same for movies recorded on the same experiment day. The residence time of each particle on the surface was calculated as the time (in seconds) that the particle had been firmly bound to the surface before dissociating. Bleached particles were disregarded in the analysis by introducing a third threshold (th_medium) to discern particles of gradually decaying intensity (i.e., bleached particles) from dissociating particles. Slight particle drifts were neglected by allowing a particle to move a maximum of spot_rad = 5 pixels between two consecutive frames and still be considered as firmly bound.

Association rates were calculated by counting the number of newly arrived particles over time, constructing a cumulative plot, and calculating the slope of the linear fit of that curve (the first 150 s of the curve were disregarded for the linear fit, to discard artifacts associated with an underestimation of the number of particles detected by the software in the first frames). Dissociation events detected by the software were visually inspected to exclude events originating from diffusing particles. The final number of dissociation events was then divided by the total number of associated particles to estimate the percentage of dissociating particles. The slope of the association curves was averaged over $n \geq 3$ observations (see Table S2 for complete statistical information) and reported with standard deviations. Association rates per GAG were calculated by dividing the measured association rates with the concentration of virus in solution, provided by the viral DNA count (in molar), and the surface density of GAG chains. The use of the viral DNA count as the particle concentration of the virus suspension assumes that each virus particle comprises one copy of viral DNA. This is considered accurate, since the vast majority of virions comprise one DNA-containing capsid, as observed by electron microscopy (data not shown).

Fluorescence recovery after photobleaching

The surfaces were functionalized as described above but using fluorescently labeled SA (Alexa Fluor 488 conjugate). SA was photobleached using green laser (532 nm) illumination for a total duration of 2 s. Movies were recorded for a minimal duration of 20 min after photobleaching and analyzed using in-house written MATLAB scripts (55).

RESULTS AND DISCUSSION

GAG surface immobilization

To study HSV-1/GAG interactions, a biomimetic surface consisting of GAG chains end-grafted onto sensor surfaces (35,56,57) was implemented. The platform was constructed taking advantage of the high binding affinity between biotin

and SA to attach reducing-end-biotinylated GAGs to an SA-modified surface. In this case, a biotinylated supported lipid bilayer (SLB) was used as support (Fig. 1 *A*).

The GAGs used in this study were HA, a synthetically sulfated version of HA (sHA), CS, and HS. HA is the only nonsulfated GAG in this study and is used here as a negative control to demonstrate the specificity of the HSV interaction to sulfate groups. To study the influence of the degree of sulfation and arrangement of sulfate groups along the GAG chain, we compared the two native GAGs CS and HS to synthetically sulfated sHA. sHA differs from the native CS and HS in several aspects. First of all, sHA presents on average two to three times more sulfate groups than CS and HS (see Table 1). Second, the chemical sulfation of GAGs occurs in a more random fashion, depending on the sulfation probability of each site on the saccharide ring, likely to result in a rather homogeneous distribution of the sulfate groups along the chains. This contrasts with the highly heterogeneous distribution of the sulfate groups on the native GAG chains (22), likely to present alternating sulfate patterns along their chains, especially for HS (25).

The surface modification process was monitored in real time using MP-SPR sensing. A typical sensorgram is shown in Fig. 1 *B* whereas the angular shifts of the SPR response for all binding steps and the estimated optical mass, surface coverage (chain density), and chain-to-chain distance for the GAG immobilization are given in Table 2.

From the SPR responses of the GAG-binding step at saturation (Fig. 1 *B*, *iii*), we observed that the different GAGs yielded different surface coverage values on the sensor surface. The highest coverage was obtained for HS. In comparison, ~13, ~21, and ~63% of this coverage was obtained for CS, sHA, and HA, respectively. The measured values of surface coverage were in agreement with previous studies (35,58).

GAG-bound virus particles exhibit lateral diffusion

To study the characteristics of HSV-1 binding to the different GAGs, TIRF microscopy was used to visualize individual GAG-bound HSV virions and to investigate their diffusive behavior and interaction kinetics. These experiments were carried out after fluorescent labeling of the virions with a cell membrane dye (59) and adding them to GAG-modified surfaces. Time-lapse movies were acquired after equilibration but without rinsing. Thanks to the TIR setup of the microscope, only fluorophores in close proximity (100–200 nm) to the surface were excited while the fluorescent background was effectively suppressed, making it possible to discriminate surface-bound virions from the ones in solution. A typical TIRF image of HSV-1 bound to CS is shown in Fig. 2 *A* (see Supporting Material for movie files). To demonstrate the specificity of the HSV-1 interaction to sulfated GAGs, we tested virus binding to (nonsulfated) HA, which resulted in significantly reduced virus attachment (Fig. 2 *B*).

Visual inspection of the recorded movies indicated that a fraction of HSV-1 particles bound to the GAG adlayer undergo a lateral movement. To characterize the observed virus mobility, time-lapse movies were recorded at 0.67 fps for a total duration of ~19 min and analyzed by SPT. The extracted mean-square displacement (MSD) curves (see MSD curves in Figs. S3 and S4, for example), calculated from single-particle trajectories (Fig. 3, *A* and *B*), showed indications of anomalous diffusion for a notable fraction of HSV-1 trajectories (i.e., MSDs showing nonlinear dependence of Δt), requiring the fitting of the MSD curves using normal and anomalous diffusion models to determine the diffusion coefficients, D (see Materials and Methods for details). Histograms of the determined D distributions were dominated by a peak at 0.5×10^{-7} or at 1×10^{-6} $\mu m^2/s$ for normal and anomalous diffusion, respectively (see Fig. S5; Fig. 3 *C*). For both diffusion modes, this peak was attributed to immobile HSV-1 virions, as its nonzero value can be fully explained by the localization noise of our SPT setup (see Supporting Material). Besides this, an additional peak was observed at higher D values, being on the order of 10^{-6} to 10^{-5} $\mu m^2/s$ for normal diffusion and ranging between 10^{-4} and 10^{-3} $\mu m^2/s$ for anomalous diffusion. These values are two to three orders of magnitude larger than the apparent D of immobile virions and thus are clearly indicative of diffusing HSV-1 particles (see Figs. S3

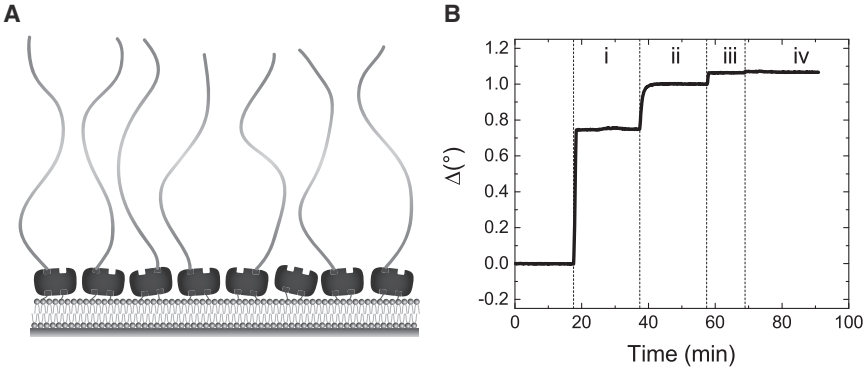

FIGURE 1 (*A*) Illustration showing the end-grafted immobilization of GAG chains onto SA molecules bound to a supported lipid bilayer. (*B*) SPR sensorgram (surface plasmon excitation at 670 nm) showing the different binding steps for GAG immobilization: SLB formation (*i*), SA binding (*ii*), GAG immobilization (HA shown here; *iii*), and rinsing (*iv*).

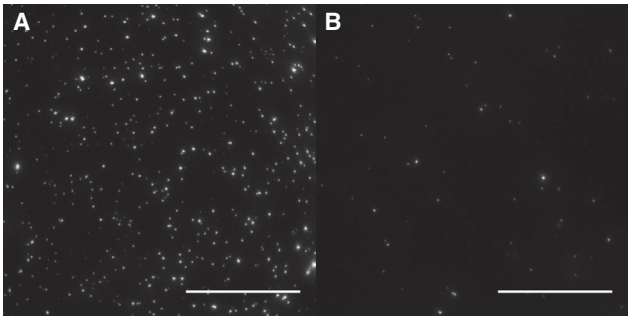

FIGURE 2 TIRF image of fluorescently labeled HSV-1 particles on a CS (*A*) and a (nonsulfated) HA surface (*B*). Scale bars represent 50 μm.

and S4, *insets*, for representative HSV-1 trajectories), as the corresponding *D* values cannot be explained taking only localization noise into consideration. Hence, although the HSV-1 particle diffusion coefficients appear to be relatively small, the virions clearly move beyond the resolution limit of our SPT setup and are, in addition, on the same order of magnitude as previously reported diffusion coefficients of cell-surface-bound nonviral vectors (60).

The peaks corresponding to mobile and immobile HSV-1 particles always showed broad distributions, with diffusion coefficients spanning at least one order of magnitude (Fig. 3 *C*). For example, *D* values in the mobile peak distribution of anomalous diffusion could reach up to 0.1 $\mu m^2/s$, resulting in a lateral diffusion that is visible by eye on the recorded movies (Fig. 3, *A* and *B*). To provide a quantitative estimate of the normal and anomalous diffusion coefficients for virions bound to different GAG types (Table 3), the peak coefficients were determined using log-normal fitting, i.e., by fitting Gaussian distributions to logarithmically binned *D* histograms. This was implemented in a two-step approach by fitting first the peak associated to immobile virions, which dominated the *D* histogram, followed by fitting the tail of the distribution again with a Gaussian function while keeping the parameters of the first fit fixed. Such a procedure has the advantage that no fixed cutoff value for *D* has to be defined to distinguish the immobile from the mobile fraction, allowing the *D* distributions of both populations to be determined without manual intervention. This finally yielded for each peak its average value (equal to the peak position in the *D* histogram) and mean $\pm$ SE.

The anomalous diffusion behavior showed a trend for higher diffusion coefficients on the native CS and HS in comparison to artificially sulfated sHA (Fig. 3 *D*), whereas no statistically significant changes in peak *D* value were observed for the normal diffusion. Since the mobile peak of the distribution of diffusion coefficients for anomalous diffusion was found to be one to two orders of magnitude higher than for normal diffusion, the overall fastest diffusion was indeed measured on the two native GAGs. This is in agreement with our qualitative visual observations revealing a fraction of highly mobile virions on the native GAGs (see Supporting Material for movie files).

It is important to note that the fluid nature of the underlying SLBs can result in mobile SA and, consequently, mobile GAG chains. Fluorescence recovery after photobleaching (FRAP) experiments (with SLBs containing 1% biotinylated lipids)

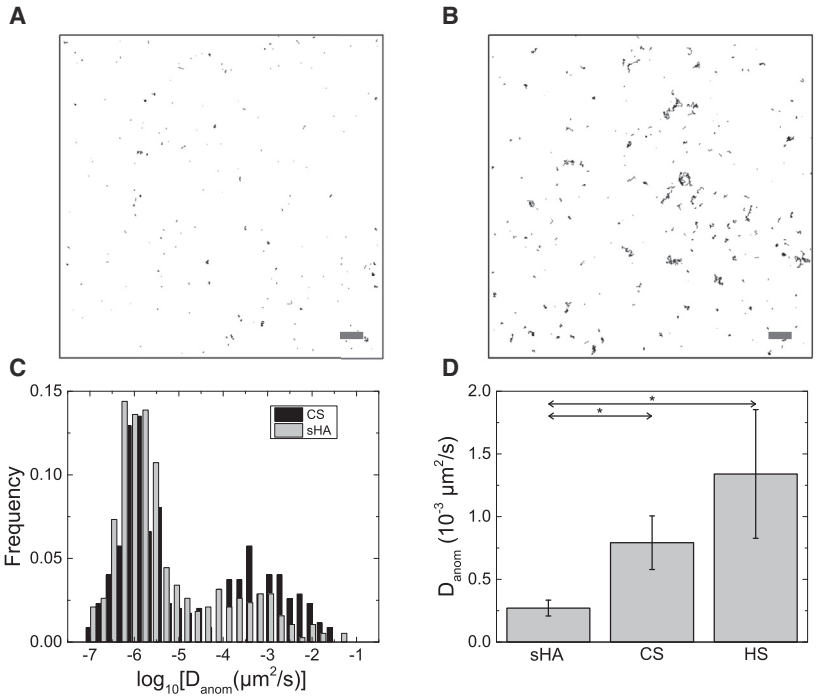

FIGURE 3 SPT quantifies virus mobility on different GAG surfaces. (*A* and *B*) Mobile tracks ($D > 3.2 \times 10^{-5}$ $\mu m^2/s$ for anomalous diffusion and $D > 1 \times 10^{-6}$ $\mu m^2/s$ for normal diffusion) for a representative sHA (*A*) and CS (*B*) surface. Scale bars represent 10 μm. (*C*) Histogram of diffusion coefficients for particles undergoing anomalous diffusion on a CS and sHA surface. (*D*) Mobile peak *D* values (anomalous diffusion) for sHA, CS, and HS, showing a trend toward higher diffusion coefficients for native GAGs. Significant shifts ($*p < 0.05$) are indicated.

TABLE 3 Comparison of Peak Diffusion Coefficients and Mobile Fractions of Virus Particles for Different GAGs

	Anomalous Diffusion			Normal Diffusion			
	D (10^{-6} $\mu m^2/s$) Immobile Peak	D (10^{-4} $\mu m^2/s$) Mobile Peak	Mobile Fraction	D (10^{-8} $\mu m^2/s$) Immobile Peak	D (10^{-6} $\mu m^2/s$) Mobile Peak	Mobile Fraction	Fraction of Particles Assigned to Anomalous Diffusion
sHA	1.19 ± 0.07	2.71 ± 0.63	0.35 ± 0.07	4.66 ± 0.42	10.3 ± 1.78	0.39 ± 0.11	0.20 ± 0.03
CS	1.06 ± 0.11	7.92 ± 2.14	0.46 ± 0.05	5.27 ± 0.31	8.42 ± 1.28	0.34 ± 0.07	0.21 ± 0.04
HS	1.21 ± 0.14	13.4 ± 5.13	0.37 ± 0.07	6.00 ± 1.46	5.47 ± 2.11	0.39 ± 0.17	0.25 ± 0.05

estimated the immobile fraction of adsorbed SA molecules as 55.6 ± 2.5%, whereas the remaining SA molecules had an average diffusion coefficient of 0.67 ± 0.02 $\mu m^2/s$; diffusion was not affected by the type of bound GAG chain. Hence, the observed HSV-1 mobility can be caused either by diffusion of the GAG chains alone, by transient attachment/detachment of HSV-1 to different GAG chains (allowing it to move at the interface while being firmly linked to it), or by a mixture of both. It is, however, very unlikely that the HSV-1 mobility stems from GAG chain mobility alone: As the GAG chain mobile fraction is <50%, an average interaction of two GAG chains per HSV-1 leads to an expected mobile fraction of 25% (50 × 50%) that is already below the experimental value of ~35% (Table 3), observed irrespective of the diffusive mode. Interacting with two GAG chains, each of which has an average D value of 0.67 $\mu m^2/s$ is, however, not sufficient to quantitatively explain the range of the small HSV-1 D values observed in the diffusion coefficient distributions (Fig. 3 *C*); (61–63).

Although it appears unlikely that the HSV-1 mobility is caused by mobile GAG chains alone, additional experiments were performed to elucidate the actual role of GAG chain mobility. First, in an attempt to decrease the mobile fraction of SA, we increased the amount of biotinylated lipids in the SLB from 1 to 5%. With this system, the recovery of the bleached spot was drastically reduced (see Fig. S6) and the immobile fraction of GAG chains increased to 86.4 ± 2.7%; the remaining mobile fraction had an average diffusion coefficient of 0.11 ± 0.06 $\mu m^2/s$. Despite this drastic reduction in GAG chain mobility, the diffusive behavior of HSV-1 was widely unaffected (Fig. S7 *A*), indicating that the GAG chain mobility has little influence on the HSV-1 mobility under the given experimental conditions. In a second approach, we exchanged the underlying SLB with a PLL-g-PEG layer containing 10% of PEG-biotin, previously used for similar surface modifications (64). The advantage of this approach is the complete absence of diffusing GAG chains (65,66). Although interacting with fully immobile GAG chains, mobile HSV-1 tracks, strongly resembling the ones obtained using SLBs, were still recorded (Fig. S7 *B*), proving that the observed HSV-1 mobility is a consequence of transient interactions with GAGs and not due to diffusion of GAG chains alone. Nevertheless, the anti-fouling properties of this system were inferior in comparison to the SLB surfaces, yielding higher amounts of nonspecific binding, as verified using HA (~30% of binding to HA, compared to ~10% with the bilayer system). This further justifies the choice of SLBs for our investigations.

Taken together, our results strongly suggest that the observed mobility of HSV-1 on the immobilized GAG surfaces is caused by multivalently attached virions undergoing a lateral "wobbling" movement caused by the disruption and reformation of single bonds with the surface (28). This interpretation is further supported by the presence of anomalous diffusion, which requires broad distributions of the release times (i.e., the time required to release a bound virus) (67), a feature previously observed when studying virus release kinetics (29,68).

It is not yet clear why the movement of certain HSV-1 particles can be well described by normal diffusion, whereas others require anomalous diffusion. Diffusion was only observed for a sub-population of the studied virus sample. This could be, among others, a consequence of the heterogeneity of the virus suspension. Indeed, most viral suspensions are composed of distinct subpopulations, characterized, for example, by different size characteristics or expression of glycoproteins. Previous studies have shown that these viral subpopulations can demonstrate differences in infectivity (69). Although it is at this stage not possible to determine whether the fraction of mobile HSV-1 virions also presents higher infectivity, the high abundance of GAGs in the extracellular matrix and close to the cell surface could provide the means for HSV-1 diffusion in vivo.

Our results indicate that the mobility of HSV-1 particles showing anomalous diffusion is enhanced on CS and HS layers in comparison to sHA. To interpret this, one has to consider the differences in chain and sulfate group density of the GAG surfaces, as the diffusive behavior of the virions is likely to be influenced by these two factors. As reported in Table 2, the highest chain density was measured for HS and was four to five times higher than that measured for sHA. The density of sulfate groups was in the same range for HS and sHA and ~6 times higher than for CS. If the differences in measured diffusion were originating solely from the differences in chain and sulfate density, we would expect the diffusion of HSV to be slowest on the HS surface, since a higher chain and sulfate density would theoretically result in a higher number of bonds created between the virion and the GAG surface, and therefore to slower diffusion. The increase in measured D values on native CS and HS in comparison to artificially sulfated sHA therefore suggests that the diffusion coefficient depends on the nature of the GAG chain,

and that the arrangement and patterns of sulfation along the native GAG chains may influence the virus mobility. Such a trend is not resolved for HSV-1 particles showing normal diffusion, either due to lack of resolution in D determination or to differences in the interaction mode that finally lead to different diffusive behaviors. It should be noted that the SPT analysis does not provide information about the z position of the virions, i.e., how much the virion penetrates into the glycan layer. In our case, the length of the GAGs was only about one-tenth to one-fifth of the virus diameter, indicating that the virus does not significantly penetrate into the GAG layer and that entanglement with the polymer chain is unlikely to significantly affect the observed diffusive behavior.

The lateral diffusion of single HSV particles on the GAG surfaces and the observed dependence on degree of sulfation and arrangement of sulfate groups could be of importance in understanding the contribution of different types of GAGs to the initial attachment of virions at the cell surface. It can be hypothesized that the mobile virions can take advantage of differences in GAG types and charge gradients induced by burst-like appearances of highly sulfated stretches of the HS/CS chains in the glycocalyx (20) to "stochastically roll" toward the cell surface while relying on its ability to break and reform single GAG-bonds. Our findings further suggest that the initial attachment of HSV-1 to GAGs exposed on the cell membrane could be a dynamic process in which viruses move in a two-dimensional plane in search of secondary receptors before firmly attaching to the membrane and proceeding with viral entry, as reported for other viruses (70–72). This hypothesis and the importance of this motion behavior during viral entry will be the subject of further investigation involving live-cell experiments.

The degree of sulfation and arrangement of sulfate groups along the GAG chain influences the HSV/GAG interaction kinetics

To study interaction kinetics of single HSV-1 particles with the immobilized GAGs, we further used TIRF-based equilibrium fluctuation analysis (30). In this method, both the rate of arriving particles over time and their individual residence times are determined, allowing for the extraction of both association and dissociation rate constants of fluorescently labeled HSV-1 particles to and from the GAG surface.

To gain insights into the association behavior of single HSV-1 particles to the different GAG surfaces, we consider the cumulative number of newly bound particles over time as shown in Fig. 4 *A* for the three sulfated GAGs as well as for HA (negative control). Virus binding was observed for all three sulfated GAGs, whereas only a few particles bound to the nonsulfated HA (~10% of the association rate on sHA), thereby confirming the specificity of the HSV-1 interaction to sulfated GAGs. Association rates to sHA, CS, and HS, calculated as the slopes of the cumulative number of newly bound particles over time, appear to be in a similar range, but with significantly more particles binding to CS than to sHA (Fig. 4 *B*).

Under the assumption that the binding kinetics are reaction-limited, the association rate (i.e., the slope of the cumulative plot shown in Fig. 4 *A*) is directly proportional to the association rate constant, k_{on}, according to Eq. 4 (29):

$$\frac{d\Theta(t)}{dt} = k_{on} C \Theta_{max}, \tag{4}$$

where C is the concentration of virus particles in solution and Θ_{max} is the number of receptors on the surface. To verify whether our system is in the reaction-limited regime, we estimated minimal association rates for the diffusion-limited case using the Ilkovic model (73). For this calculation, we used the PFU count as the concentration of virus particles. This number only accounts for the number of infectious particles in the virus suspension, and therefore is an underestimation of the total number of virus particles. However, for an estimation of minimal association rates, the PFU count is better suited than the viral DNA count, since it provides the minimal amount of HSV particles likely to interact with the GAG surfaces. With the Ilkovic model for diffusion-limited kinetics, we predicted association rates that were at least one order of magnitude higher

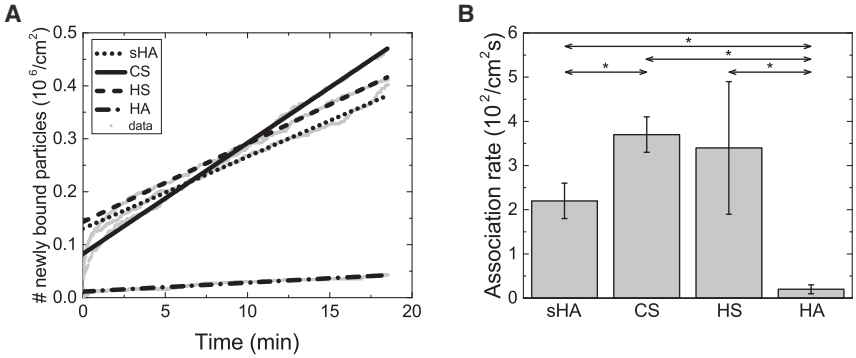

FIGURE 4 Association kinetics of single virus particles to GAG surfaces. (*A*) Cumulative plot of newly detected particles over time, including linear fits (first 150 s disregarded for the linear fits). (*B*) Measured association rates for sHA, CS, HS, and HA. Significant shifts ($*p < 0.05$) are indicated.

than the measured association rates, therefore validating the assumption of reaction-limited binding kinetics.

A calculation of the association rate constants, k_{on}, from the obtained data of association rates (Table 4) is not straightforward for complex systems like the multivalent HSV-GAG interaction, composed of multiple bonds between the viral glycoproteins and surface bound GAGs. In such multivalent systems, one usually distinguishes between affinity constants calculated for the overall interaction and affinity constants of each single bond (18). Although we previously reported binding affinities of purified gC glycoproteins from HSV-1 to end-grafted CS and sHA, measured with SPR (58), in this article, we focused on studying binding kinetics of the overall HSV-GAG interaction. For such a system, a major complication for the estimation of binding constants originates from the determination of the receptor concentration, Θ_{max}. The glycoproteins on the viral envelope are likely to bind to clusters of sulfate groups on the GAG chain, raising the question whether Θ_{max} is more accurately determined by the density of GAG chains or the density of sulfate groups. Nevertheless, in an attempt to quantify the measured association kinetics while relating it to differences in GAG chain densities, we calculated association rates per GAG by dividing the measured association rates with the concentration of HSV-1 particles in solution obtained by DNA quantification (in molar) and the surface coverage (of GAGs) (Table 2), in analogy with Eq. 4, but using the chain density as a value for Θ_{max}. These calculations (Table 4) show that the highest binding propensities were obtained for native CS, with on average ~3 times more particles per GAG binding to CS in comparison to sHA. This enhanced association behavior could be an indication for a preference of HSV to bind to specific arrangements of sulfates on native GAGs, as opposed to more homogeneously distributed sulfates on sHA. The surprisingly low association rate to HS (~10% of CS association per GAG) could, at least partially, be explained by the high chain density of HS. Indeed, the average chain-to-chain density for this GAG was calculated to be ~7 nm (Table 2), which is shorter than the estimated mean spacing between glycoprotein spikes on the viral envelope of ~13 nm (39). It is therefore likely that after exceeding a certain threshold, association is not enhanced anymore for higher chain densities. The limiting factor of this interaction then becomes the number of viral glycoproteins, resulting in reduced association rates per HS chain.

TABLE 4 Association Rates and Corresponding Association Rate per Sulfate Group Estimations for the Different GAG Surfaces

	Association Rate (10^2/cm^{2}s)	Association Rate per GAG (10^2/Ms)
sHA	2.2 ± 0.4	12.5 ± 3.2
CS	3.7 ± 0.4	40.2 ± 17.5
HS	3.4 ± 1.5	4.1 ± 1.9
HA	0.2 ± 0.1	0.47 ± 0.16

From the analysis of the recorded movies, it appeared that only very few virus particles dissociated from the surface, indicating that once bound, the virions can undergo lateral movements while being trapped on the GAG surface. Indeed, for all investigated GAGs, <0.5% of the bound particles were observed to leave the surface for the duration of the experiment. This interesting result, further confirmed by longer time series (1 h), shows that complete dissociation events, which would require the virus particle to break all of the bonds with the GAG layer within a very short time period in which no new bond would be formed, are very unlikely and therefore rarely observed. It also suggests that GAGs are very efficient at recruiting HSV particles in the extracellular matrix and at the cell surface.

Taken together, HSV-GAG interaction kinetics showed increased HSV-1 association rates to native CS in comparison to chemically sulfated sHA, which could not be explained by differences in chain density or degree of sulfation of the GAG chain, therefore suggesting a preference of HSV-1 to specific arrangements of sulfates on native GAGs. Furthermore, very low dissociation rates were observed from all GAG surfaces. These results suggest higher overall binding affinities of the virus to CS in comparison to sHA, which contrasts with the observed faster diffusion of HSV-1 on CS in comparison to sHA. This illustrates the complexity of multivalent virus-GAG interactions, which are characterized not only by overall binding affinities but also by the reaction constants of the individual bonds (glycoprotein/GAG bonds in the case of HSV-1). Our previous investigations on purified gC glycoproteins (58) did not reveal any significant differences in apparent binding affinities of gC to CS or chemically sulfated sHA, although they did not exclude that the gC/CS and gC/sHA bonds may differ in their association and dissociation constants, k_{on} and k_{off}. We observed complex overshooting binding behaviors of gC to end-grafted GAG chains, complicating the quantitative analysis of k_{on} and k_{off} (58). However, our data, presented in Fig. S8, clearly indicate that gC has a higher propensity to dissociate from the CS layer than from sHA. This observation indicates that the gC/CS interaction is more dynamic than gC/sHA, resulting in a higher propensity of HSV to break and reform single bonds with the CS layer. This characteristic is likely to confer a higher surface sampling capability to the virus, which might explain the observed differences in HSV mobility.

CONCLUSION

In this study, we used SPT and equilibrium fluctuation analysis to study interaction kinetics and lateral mobility of single HSV-1 particles on end-grafted GAGs. Our results showed that HSV-1 efficiently binds to native CS and HS, and to the artificially sulfated sHA, but not to nonsulfated HA. Once bound to the GAG layer, the virions appeared to be trapped while undergoing lateral diffusion on the

GAG chains. Furthermore, our experiments showed a tendency toward higher diffusion coefficients on the native CS and HS surfaces in comparison to sHA. These results indicate that the degree of sulfation, but also the arrangement of sulfate groups along the GAG chain, influence HSV mobility. Taken together, our findings therefore suggest that the physicochemical properties of cell-surface GAGs could play a determining role in modulating the different steps leading to virus uptake by a host cell.

SUPPORTING MATERIAL

Supporting Materials and Methods, eight figures, two tables, and four movies are available at http://www.biophysj.org/biophysj/supplemental/S0006-3495(17)30678-1.

AUTHOR CONTRIBUTIONS

M.B. and T.B. conceived and coordinated this study, with help from E.T. M.B. and N.P. designed the experiments. All included experiments and data analyses were carried out by N.P. N.A. performed preliminary experiments leading up to this project. S.B. wrote the MATLAB scripts for SPT analysis and helped with parts of the analysis. O.W. wrote the MATLAB scripts for equilibrium fluctuation analysis. The GAG surface modification strategy was developed by N.A. S.M. and M.S. prepared the biotinylated GAG derivatives HA, sHA, and CS. The manuscript was written mainly by N.P., S.B., and M.B, with improvements and suggestions from all authors. All authors read and approved the manuscript.

ACKNOWLEDGEMENTS

The authors acknowledge Prof. Ralf P. Richter and Dr. Dhruv Thakar for providing HS material, Prof. Fredrik Höök for fruitful discussions, Maria Johansson for support with virus purification and quantification, and Mokhtar Mapar for help with data evaluation.

The Swedish Research Council (Vetenskapsrådet, 621-2012-5024 to M.B.), the Marie Curie Actions, the Area of Advance Materials (Materials for Health, Chalmers), and the Focus Area Nanoscale (Freie Universität Berlin) are acknowledged for financial support. M.S. and S.M. acknowledge financial support from the German Research Council (DFG, TR 67, project A2).

SUPPORTING CITATIONS

References (52,58,62) appear in the Supporting Material.

REFERENCES

1. Olofsson, S., and T. Bergström. 2005. Glycoconjugate glycans as viral receptors. *Ann. Med.* 37:154–172.
2. Saphire, A. C. S., M. D. Bobardt, …, P. A. Gallay. 2001. Syndecans serve as attachment receptors for human immunodeficiency virus type 1 on macrophages. *J. Virol.* 75:9187–9200.
3. Salvador, B., N. R. Sexton, …, G. Simmons. 2013. Filoviruses utilize glycosaminoglycans for their attachment to target cells. *J. Virol.* 87:3295–3304.
4. Giroglou, T., L. Florin, …, M. Sapp. 2001. Human papillomavirus infection requires cell surface heparan sulfate. *J. Virol.* 75:1565–1570.
5. Kim, S. Y., J. Zhao, …, R. J. Linhardt. 2017. Interaction of Zika virus envelope protein with glycosaminoglycans. *Biochemistry.* 56:1151–1162.
6. Corey, L., and P. G. Spear. 1986. Infections with herpes simplex viruses (1). *N. Engl. J. Med.* 314:686–691.
7. Fatahzadeh, M., and R. A. Schwartz. 2007. Human herpes simplex virus infections: epidemiology, pathogenesis, symptomatology, diagnosis, and management. *J. Am. Acad. Dermatol.* 57:737–763, quiz 764–766.
8. Herold, B. C., D. WuDunn, …, P. G. Spear. 1991. Glycoprotein C of herpes simplex virus type 1 plays a principal role in the adsorption of virus to cells and in infectivity. *J. Virol.* 65:1090–1098.
9. Banfield, B. W., Y. Leduc, …, F. Tufaro. 1995. Evidence for an interaction of herpes simplex virus with chondroitin sulfate proteoglycans during infection. *Virology.* 208:531–539.
10. Mårdberg, K., E. Trybala, …, T. Bergström. 2002. Herpes simplex virus type 1 glycoprotein C is necessary for efficient infection of chondroitin sulfate-expressing gro2C cells. *J. Gen. Virol.* 83:291–300.
11. Herold, B. C., R. J. Visalli, …, P. G. Spear. 1994. Glycoprotein C-independent binding of herpes simplex virus to cells requires cell surface heparan sulphate and glycoprotein B. *J. Gen. Virol.* 75:1211–1222.
12. Mårdberg, K., E. Trybala, …, T. Bergström. 2001. Mutational analysis of the major heparan sulfate-binding domain of herpes simplex virus type 1 glycoprotein C. *J. Gen. Virol.* 82:1941–1950.
13. Trybala, E., T. Bergström, …, S. Olofsson. 1994. Localization of a functional site on herpes simplex virus type 1 glycoprotein C involved in binding to cell surface heparan sulphate. *J. Gen. Virol.* 75:743–752.
14. Xu, D., and J. D. Esko. 2014. Demystifying heparan sulfate-protein interactions. *Annu. Rev. Biochem.* 83:129–157.
15. Feyzi, E., E. Trybala, …, D. Spillmann. 1997. Structural requirement of heparan sulfate for interaction with herpes simplex virus type 1 virions and isolated glycoprotein C. *J. Biol. Chem.* 272:24850–24857.
16. Herold, B. C., S. I. Gerber, …, K. Holme. 1995. Identification of structural features of heparin required for inhibition of herpes simplex virus type 1 binding. *Virology.* 206:1108–1116.
17. Collins, B. E., and J. C. Paulson. 2004. Cell surface biology mediated by low affinity multivalent protein-glycan interactions. *Curr. Opin. Chem. Biol.* 8:617–625.
18. Mammen, M., S. K. Choi, and G. M. Whitesides. 1998. Polyvalent interactions in biological systems: implications for design and use of multivalent ligands and inhibitors. *Angew. Chemie-International.* 37:2754–2794.
19. Ewers, H., V. Jacobsen, …, V. Sandoghdar. 2007. Label-free optical detection and tracking of single virions bound to their receptors in supported membrane bilayers. *Nano Lett.* 7:2263–2266.
20. Esko, J. D., K. Kimata, and U. Lindahl. 2009. Proteoglycans and sulfated glycosaminoglycans. *In* Essentials of Glycobiology. A. Varki, R. D. Cummings, J. D. Esko, H. H. Freeze, P. Stanley, C. R. Bertizzo, G. W. Hart, and M. E. Etzler, editors. Cold Spring Harbor Laboratory Press, pp. 229–248.
21. Spillmann, D. 2001. Heparan sulfate: anchor for viral intruders? *Biochimie.* 83:811–817.
22. Lamanna, W. C., I. Kalus, …, T. Dierks. 2007. The heparanome—the enigma of encoding and decoding heparan sulfate sulfation. *J. Biotechnol.* 129:290–307.
23. Fernaud-Espinosa, I., M. Nieto-Sampedro, and P. Bovolenta. 1996. Developmental distribution of glycosaminoglycans in embryonic rat brain: relationship to axonal tract formation. *J. Neurobiol.* 30:410–424.
24. Sasisekharan, R., Z. Shriver, …, U. Narayanasami. 2002. Roles of heparan-sulphate glycosaminoglycans in cancer. *Nat. Rev. Cancer.* 2:521–528.
25. Gama, C. I., and L. C. Hsieh-Wilson. 2005. Chemical approaches to deciphering the glycosaminoglycan code. *Curr. Opin. Chem. Biol.* 9:609–619.
26. Raman, R., V. Sasisekharan, and R. Sasisekharan. 2005. Structural insights into biological roles of protein-glycosaminoglycan interactions. *Chem. Biol.* 12:267–277.

27. Costello, D. A., J. K. Millet, …, S. Daniel. 2013. Single particle assay of coronavirus membrane fusion with proteinaceous receptor-embedded supported bilayers. *Biomaterials.* 34:7895–7904.

28. Kukura, P., H. Ewers, …, V. Sandoghdar. 2009. High-speed nanoscopic tracking of the position and orientation of a single virus. *Nat. Methods.* 6:923–927.

29. Bally, M., A. Gunnarsson, …, F. Höök. 2011. Interaction of single viruslike particles with vesicles containing glycosphingolipids. *Phys. Rev. Lett.* 107:188103.

30. Gunnarsson, A., P. Jönsson, …, F. Höök. 2008. Single-molecule detection and mismatch discrimination of unlabeled DNA targets. *Nano Lett.* 8:183–188.

31. Gunnarsson, A., L. Dexlin, …, F. Höök. 2011. Kinetics of ligand binding to membrane receptors from equilibrium fluctuation analysis of single binding events. *J. Am. Chem. Soc.* 133:14852–14855.

32. Kunze, R., M. Rösler, …, P. Dieter. 2010. Sulfated hyaluronan derivatives reduce the proliferation rate of primary rat calvarial osteoblasts. *Glycoconj. J.* 27:151–158.

33. Hintze, V., S. Moeller, …, D. Scharnweber. 2009. Modifications of hyaluronan influence the interaction with human bone morphogenetic protein-4 (hBMP-4). *Biomacromolecules.* 10:3290–3297.

34. Thakar, D., E. Migliorini, …, R. P. Richter. 2014. A quartz crystal microbalance method to study the terminal functionalization of glycosaminoglycans. *Chem. Commun. (Camb.).* 50:15148–15151.

35. Altgärde, N., E. Nilebäck, …, S. Svedhem. 2013. Probing the biofunctionality of biotinylated hyaluronan and chondroitin sulfate by hyaluronidase degradation and aggrecan interaction. *Acta Biomater.* 9:8158–8166.

36. Holland, T. C., S. D. Marlin, …, J. Glorioso. 1983. Antigenic variants of herpes simplex virus selected with glycoprotein-specific monoclonal antibodies. *J. Virol.* 45:672–682.

37. Trybala, E., J. A. Liljeqvist, …, T. Bergström. 2000. Herpes simplex virus types 1 and 2 differ in their interaction with heparan sulfate. *J. Virol.* 74:9106–9114.

38. Namvar, L., S. Olofsson, …, M. Lindh. 2005. Detection and typing of Herpes Simplex virus (HSV) in mucocutaneous samples by TaqMan PCR targeting a gB segment homologous for HSV types 1 and 2. *J. Clin. Microbiol.* 43:2058–2064.

39. Grünewald, K., P. Desai, …, A. C. Steven. 2003. Three-dimensional structure of herpes simplex virus from cryo-electron tomography. *Science.* 302:1396–1398.

40. Jung, L. S., C. T. Campbell, …, S. S. Yee. 1998. Quantitative interpretation of the response of surface plasmon resonance sensors to adsorbed films. *Langmuir.* 14:5636–5648.

41. De Feijter, J., J. Benjamins, and F. Veer. 1978. Ellipsometry as a tool to study the adsorption behavior of syntetic and biopolyers at the air water interface. *Biopolymers.* 17:1759–1772.

42. Rupert, D. L. M., G. V. Shelke, …, F. Höök. 2016. Dual-wavelength surface plasmon resonance for determining the size and concentration of sub-populations of extracellular vesicles. *Anal. Chem.* 88:9980–9988.

43. Merz, C., W. Knoll, …, E. Reimhult. 2008. Formation of supported bacterial lipid membrane mimics. *Biointerphases.* 3:FA41–FA50.

44. Satoh, A., T. Toida, …, I. Matsumoto. 2000. New role of glycosaminoglycans on the plasma membrane proposed by their interaction with phosphatidylcholine. *FEBS Lett.* 477:249–252.

45. Hokputsa, S., K. Jumel, …, S. E. Harding. 2003. Hydrodynamic characterisation of chemically degraded hyaluronic acid. *Carbohydr. Polym.* 52:111–117.

46. Horkay, F., P. J. Basser, …, E. Geissler. 2012. Chondroitin sulfate in solution: effects of mono- and divalent salts. *Macromolecules.* 45:2882–2890.

47. DeAngelis, P. L., N. S. Gunay, …, R. J. Linhardt. 2002. Identification of the capsular polysaccharides of Type D and F *Pasteurella multocida* as unmodified heparin and chondroitin, respectively. *Carbohydr. Res.* 337:1547–1552.

48. Tumolo, T., L. Angnes, and M. S. Baptista. 2004. Determination of the refractive index increment (d*n*/d*c*) of molecule and macromolecule solutions by surface plasmon resonance. *Anal. Biochem.* 333:273–279.

49. Pavlov, G., S. Finet, …, C. Ebel. 2003. Conformation of heparin studied with macromolecular hydrodynamic methods and x-ray scattering. *Eur. Biophys. J.* 32:437–449.

50. Perez Sanchez, H., K. Tatarenko, …, C. Ebel. 2006. Organization of human interferon gamma-heparin complexes from solution properties and hydrodynamics. *Biochemistry.* 45:13227–13238.

51. Meijering, E., O. Dzyubachyk, and I. Smal. 2012. Methods for cell and particle tracking. *Methods Enzymol.* 504:183–200.

52. Saxton, M. J. 1997. Single-particle tracking: the distribution of diffusion coefficients. *Biophys. J.* 72:1744–1753.

53. Kusumi, A., Y. Sako, and M. Yamamoto. 1993. Confined lateral diffusion of membrane receptors as studied by single particle tracking (nanovid microscopy). Effects of calcium-induced differentiation in cultured epithelial cells. *Biophys. J.* 65:2021–2040.

54. Lommerse, P. H. M., G. A. Blab, …, T. Schmidt. 2004. Single-molecule imaging of the H-ras membrane-anchor reveals domains in the cytoplasmic leaflet of the cell membrane. *Biophys. J.* 86:609–616.

55. Jönsson, P., M. P. Jonsson, …, F. Höök. 2008. A method improving the accuracy of fluorescence recovery after photobleaching analysis. *Biophys. J.* 95:5334–5348.

56. Attili, S., and R. P. Richter. 2012. Combining colloidal probe atomic force and reflection interference contrast microscopy to study the compressive mechanics of hyaluronan brushes. *Langmuir.* 28:3206–3216.

57. Migliorini, E., D. Thakar, …, R. P. Richter. 2014. Well-defined biomimetic surfaces to characterize glycosaminoglycan-mediated interactions on the molecular, supramolecular and cellular levels. *Biomaterials.* 35:8903–8915.

58. Altgärde, N., C. Eriksson, …, M. Bally. 2015. Mucin-like region of Herpes simplex virus type 1 attachment protein glycoprotein C (gC) modulates the virus-Glycosaminoglycan interaction. *J. Biol. Chem.* 290:21473–21485.

59. Horan, P. K., M. J. Melnicoff, …, S. E. Slezak. 1990. Fluorescent cell labeling for in vivo and in vitro cell tracking. *Methods Cell Biol.* 33:469–490.

60. Bausinger, R., K. von Gersdorff, …, A. Zumbusch. 2006. The transport of nanosized gene carriers unraveled by live-cell imaging. *Angew. Chem. Int. Ed. Engl.* 45:1568–1572.

61. Evans, E., and E. Sackmann. 1988. Translational and rotational drag coefficients for a disk moving in a liquid membrane associated with a rigid substrate. *J. Fluid Mech.* 194:553–561.

62. Block, S., V. P. Zhdanov, and F. Höök. 2016. Quantification of multivalent interactions by tracking single biological nanoparticle mobility on a lipid membrane. *Nano Lett.* 16:4382–4390.

63. Parveen, N., S. Block, …, F. Höök. 2017. Detachment of membrane bound virions by competitive ligand binding induced receptor depletion. *Langmuir.* 33:4049–4056.

64. Sjövall, P., B. Agnarsson, …, F. Höök. 2014. Liposome binding for multiplexed biomolecule detection and imaging using ToF-SIMS. *Surf. Interface Anal.* 46:707–711.

65. Thid, D., M. Bally, …, J. Gold. 2007. Issues of ligand accessibility and mobility in initial cell attachment. *Langmuir.* 23:11693–11704.

66. Städler, B. M., C. B. Huwiler, …, H. M. Grandin. 2006. Light-induced in situ patterning of DNA-tagged biomolecules and nanoparticles. *IEEE Trans. Nanobioscience.* 5:215–219.

67. Weeks, E. R., J. S. Urbach, and H. L. Swinney. 1996. Anomalous diffusion in asymmetric random walks with a quasi-geostrophic flow example. *Physica D.* 97:291–310.

68. Nasir, W., M. Bally, …, F. Höök. 2015. Interaction of virus-like particles with vesicles containing glycolipids: kinetics of detachment. *J. Phys. Chem. B.* 119:11466–11472.

69. Bonar, M. M., and J. C. Tilton. 2017. High sensitivity detection and sorting of infectious human immunodeficiency virus (HIV-1) particles by flow virometry. *Virology.* 505:80–90.

70. Rothenberg, E., L. A. Sepúlveda, …, I. Golding. 2011. Single-virus tracking reveals a spatial receptor-dependent search mechanism. *Biophys. J.* 100:2875–2882.

71. Huang, Y.-F., G.-Y. Zhuo, …, C.-L. Hsieh. 2017. Coherent brightfield microscopy provides the spatiotemporal resolution to study early stage viral infection in live cells. *ACS Nano.* 11:2575–2585.

72. Ewers, H., A. E. Smith, …, A. Helenius. 2005. Single-particle tracking of murine polyoma virus-like particles on live cells and artificial membranes. *Proc. Natl. Acad. Sci. USA.* 102:15110–15115.

73. Dahlin, A. B. 2012. Plasmonic Biosensors: An Integrated View of Refractometric Detection. IOS Press, Amsterdam, the Netherlands, pp. 37–50.

74. Jasnin, M., L. van Eijck, …, G. Zaccai. 2010. Dynamics of heparan sulfate explored by neutron scattering. *Phys. Chem. Chem. Phys.* 12:3360–3362.